Self-Oscillating Resonant Converter With Contactless Power Transfer and Integrated Current Sensing Transformer

Ligang Xu, *Student Member, IEEE*, Qianhong Chen, *Member, IEEE*, Xiaoyong Ren, *Member, IEEE*, Siu-Chung Wong, *Senior Member, IEEE*, and Chi K. Tse, *Fellow, IEEE*

***Abstract*—In this paper, an integrated transformer is proposed to provide current sensing in the primary side and passive current phase detection for a self-oscillating contactless resonant converter (SOCRC). The proposed transformer integrates power transfer and current sensing. By using the secondary current phase of a series/series-compensated resonant converter in the control of the inverter, better output controllability, dynamic response, and self-adaptability can be achieved simultaneously. The integrated current sensing winding, being a crucial part of SOCRC, is analyzed in detail. In order to make the output voltage insensitive to the clearance and misalignment conditions, the requirement of the new integrated transformer is given. Experimental results of an 80-W SOCRC prototype verify the analytical results.**

***Index Terms*—Inductive power transfer (IPT), magnetic integration, self-oscillating resonant converter, transformer, wireless power transfer.**

I. Introduction

An inductive power transfer (IPT) system transfers power from one circuit to another through electromagnetic induction without any physical contact. It has been used in various applications ranging from a few milliwatts in biomedical applications up to several kilowatts of output power in automotive applications [1]–[4]. Due to its convenience and safety against electric shock, IPT has become increasingly popular in home appliances, mobile devices, industrial sensors, and electric vehicle (EV) chargers [5]–[7].

Although IPT systems have unique advantages in some specific applications, due to the loosely coupled transformer, the performance of an IPT system is still far from being optimal, compared to conventional power transfer systems. Moreover, the parameters of the transformer change greatly due to the need for necessary clearances and possible misalignments, leading to variation of the output performance. Therefore, the design and optimization of the IPT system under parameter variations have become an important research topic.

A great deal of research has been devoted to improve the performance of IPT systems, including coupling optimization [2], compensation method [9], [10], impedance matching [11], frequency tracking [12], [13], power flow control [14]–[16], dc/dc conversion [17], [18], etc. In [9] and [10], the series/series–parallel and series–parallel/series topologies are proposed to make the output voltage insensitive to coupling variation, respectively. In [11], a novel control method is presented to regulate the power transfer by tuning the effective resonant capacitance. In [12], a parallel-resonant Class-D oscillator is proposed, which can track the split resonant frequency automatically, so as to achieve a constant output voltage. Pulse-width-modulation phase-locked-loop control strategy is proposed in [13] to achieve output voltage control and zero-voltage switching (ZVS) at the same time. In [14], a primary side feedback method for an IPT system is proposed, using a feedback method to deal with impedance variations in the primary side when the charging path on the secondary side is being switched ON and OFF. In some specific applications, fluctuation of the load or the coupling necessitates the use of some power flow control technique, which can be implemented on either the primary or secondary side. In [15], the received power on the secondary side can be regulated by tuning or detuning the pickup on the secondary side to regulate the output power and voltage. For IPT systems with a single pickup, it is preferable to control the power flow on the primary side of the system because of the size, weight, and heat constraints [16]. To regulate the output voltage for an IPT system under parameter variations, the use of a dc/dc converter in the transmitting or receiving side is also a simple and effective approach.

Although a number of power or output voltage control strategies have been proposed, effective methods to improve the dynamic performance for IPT systems are still lacking. For some special applications, such as power supplies for CPUs and implantable devices [12], the dynamic performance is also an important consideration. Self-oscillating control is a control strategy that can achieve better dynamic response and

Manuscript received March 26, 2016; accepted July 22, 2016. Date of publication August 8, 2016; date of current version February 11, 2017. This work was supported in part by Lite-On Power Electronics Technology Research Fund, in part by the National Natural Science Foundation of China under Grant named Theory and Key Technology Research of Redundant Contactless Electronics Slip Ring Based on The Motor-slip Analog, and in part by the National Natural Science Foundation of China under Grant 51377081. Recommended for publication by Associate Editor M. Duffy.

L. Xu, Q. Chen, and X. Ren are with the Jiangsu Key Laboratory of New Energy Generation and Power Conversion, Nanjing University of Aeronautics and Astronautics, Nanjing 210016, China (e-mail: xlg324@163.com; chenqh@nuaa.edu.cn; renxy@nuaa.edu.cn).

S.-C. Wong and C. K. Tse are with the Department of Electronic and Information Engineering, The Hong Kong Polytechnic University, Kowloon, Hong Kong (e-mail: enscwong@polyu.edu.hk; michael.tse@polyu.edu.hk).

Color versions of one or more of the figures in this paper are available online at http://ieeexplore.ieee.org.

Digital Object Identifier 10.1109/TPEL.2016.2598556

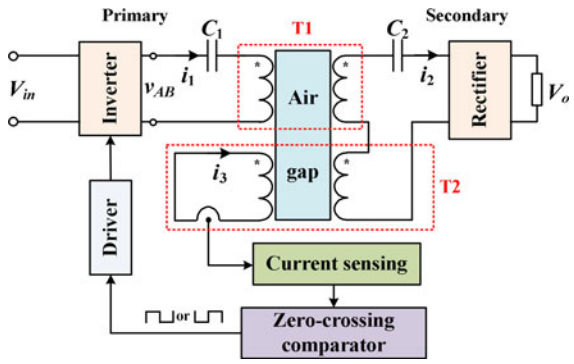

Fig. 1. Self-oscillating control diagram for SS-type CRC.

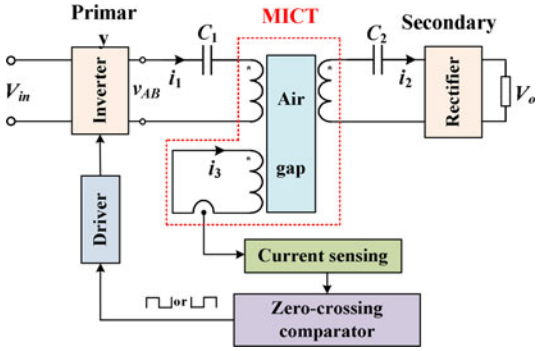

Fig. 2. Self-oscillating control diagram for SS-type CRC with MICT.

self-adaptability to parameter variations. It has been adopted in many applications such as parallel-resonant Class-D oscillators [12], series–series (SS)-type contactless resonant converters (CRC) [19], [23], and Class-E-tuned power amplifiers [22].

In [19] and [24], a self-oscillation control strategy for an SS-type CRC is proposed. A similar control concept has been adopted in [25]. The realization of self-oscillating control strategy depends on phase detection of the secondary current. In [19], a passive solution, called *phase detection contactless current transformer*, is proposed with the secondary winding shorted. Fig. 1 shows the self-oscillating control diagram for a self-oscillating contactless resonant converter (SOCRC), where T1 is the main transformer, which is used for IPT. Another current detecting transformer T2 is still needed in the system to provide the current information for the control. The requirement for T2 increases the size of the IPT system. Hence, a multifunction integrated contactless transformer (MICT) is proposed [23], as shown in Fig. 2. Compared with the structure shown in Fig. 1, MICT consists of the following three windings:

1) including primary winding;
2) secondary winding;
3) shorted current sensing winding.

However, the coupling between primary winding and the shorted current sensing winding was ignored, and no design consideration was provided in the analysis of [23].

This paper presents a complete description of the MICT, aiming to provide a more accurate analysis of its operation and control requirements. This paper is organized as follows. In Section II, the operating principle and modeling of the SS-type CRC based on the proposed MICT structure is presented.

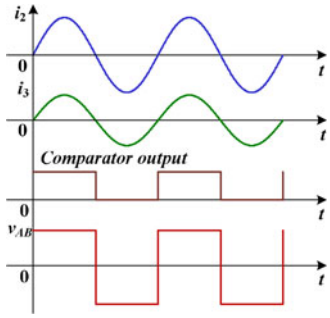

Fig. 3. Main waveforms of the self-oscillating control strategy.

Detailed discussions of the influence of the integrated current sensing winding are presented in Section III. Then, Section IV discusses the design issues of the magnetic structure of the MICT. In Section V, an experimental setup and measured results are presented. Section VI concludes the paper.

II. Operation Principles of the Proposed SOCRC With MICT

A. Review of Self-Oscillating Control Strategy

The self-oscillation control strategy for an SS-type CRC was proposed and discussed in detail in [19]. Using a transfer impedance analysis [19], it has been demonstrated that the SS-type CRC will operate at the voltage gain intersection point automatically with the gain approximately equal to the transformer's turns ratio, if the fundamental component of the inverter output voltage $v_{\rm AB}$ and the secondary current i_2 are in phase. Thus, the self-oscillating control strategy for an SS-type CRC can be designed. For the SOCRC with MICT, the self-oscillating control strategy is similar to that described in [19], as shown in Fig. 2. The control circuitry comprises the MICT, a current sensing block, a zero-crossing comparator block, and a driver block. First, the phase information of i_2 is sensed and transferred to the primary side as i_3 by the MICT. Then, i_3 can be transferred to a voltage signal by the current sensing block. Finally, the output signal of the current sensing block is converted into two complementary square waves by the zero-crossing comparator, which drive the inverter via the driver block. Neglecting the phase error due to different functional blocks, $v_{\rm AB}$ will be in phase with i_2, as shown in Fig. 3. As a result, the converter operates like a voltage follower with a gain approximately equal to the transformer's turns ratio.

As mentioned in [19], the self-oscillating control has the advantages of simplicity, better dynamic performance, and self-adaptability to parameter variations. However, it should be noted that the output voltage control is achieved indirectly as a result of the characteristics of the load-independent voltage gain, and not by the closed-loop control. Keeping the fundamental component of $v_{\rm AB}$ and i_2 in phase is the key to achieving a good output control for the SS-type CRC under the self-oscillating control. However, for the SS-type CRC with MICT, there exists a phase detection error between i_2 and i_3 and the time delay of the control or driving circuits, which will cause a hase difference between i_2 and $v_{\rm AB}$. Besides, the magnetic couplings in MICT will always affect the converter's operating point and the

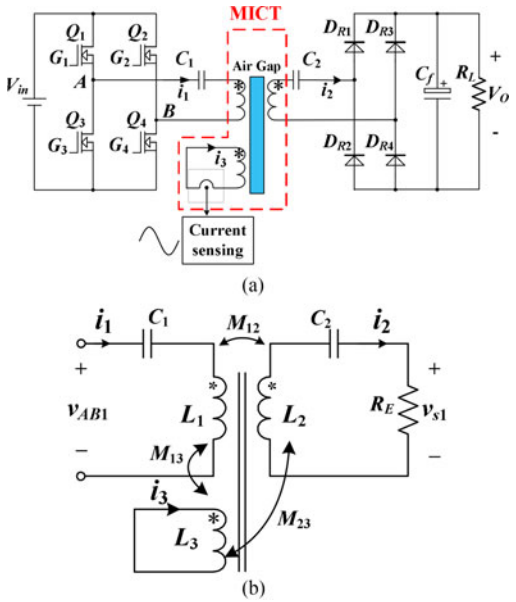

Fig. 4. (a) Topology of SOCRC with MICT. (b) Fundamental equivalent circuit of MICT.

output characteristics. Here, we provide an accurate analysis of the operation of the proposed SOCRC with MICT.

B. Characteristics of the Proposed SOCRC With MICT

In the analysis of an SS-type CRC, an approximation of the fundamental component is normally applied, since the fundamental component of the current in the resonant tank is much larger than other harmonics. Therefore, the rectifier and the load R_L can be replaced by an equivalent load R_E satisfying $R_E = (8/\pi^2)R_L$ [20]. Then, the corresponding fundamental equivalent circuit of the converter can be obtained, as shown in Fig. 4. The full-bridge inverter comprises four switches (Q_1–Q_4), which operate in complementary mode and convert a dc voltage $V_{\rm in}$ to a high-frequency ac voltage $v_{\rm AB}$. Here, C_1 and C_2 are the resonant capacitors, v_s represents the input voltage of the full-bridge rectifier, $v_{\rm AB1}$ and v_{s1} are the fundamental components of $v_{\rm AB}$ and v_s respectively. Also, L_1, L_2, and L_3 are the self-inductances of the primary, the secondary, and the current sensing windings, respectively; M_{12}, M_{13}, and M_{23} represent the mutual inductances between L_1, L_2, and L_3. The coupling coefficients k_{12}, k_{13}, and k_{23} of the transformer satisfies

$$k_{12} = M_{12}/\sqrt{L_1L_2}, k_{13} = M_{13}/\sqrt{L_1L_3} \text{ and}$$
$$k_{23} = M_{23}/\sqrt{L_2L_3}.$$

Define

$$Z_1 = j\omega L_1 + \frac{1}{j\omega C_1} \quad Z_2 = j\omega L_2 + \frac{1}{j\omega C_2} \quad Z_3 = j\omega L_3. \tag{1}$$

Applying KVL, we get

$$\begin{cases} Z_1\dot{I}_1 - j\omega M_{12}\dot{I}_2 + j\omega M_{13}\dot{I}_3 = \dot{V}_{\rm AB1} \\ j\omega M_{12}\dot{I}_1 - (Z_2 + R_E)\dot{I}_2 + j\omega M_{23}\dot{I}_3 = 0 \\ j\omega M_{13}\dot{I}_1 - j\omega M_{23}\dot{I}_2 + Z_3\dot{I}_3 = 0. \end{cases} \tag{2}$$

Consequently, we have

$$\begin{cases} \dot{I}_1 = \dfrac{(Z_2 + R_E) + (\omega M_{23})^2/Z_3}{A} \cdot \dot{V}_{\rm AB1} \\ \dot{I}_2 = \dfrac{j\omega M_{12} + \omega^2 M_{13}M_{23}/Z_3}{A} \cdot \dot{V}_{\rm AB1} \\ \dot{I}_3 = \dfrac{[-\omega^2 M_{12}M_{23} - j\omega M_{13}(Z_2 + R_E)]/Z_3}{A} \cdot \dot{V}_{\rm AB1} \end{cases} \tag{3}$$

where $A = Z_1(Z_2 + R_E) + (\omega M_{12})^2 + [Z_1(\omega M_{23})^2 + (Z_2 + R_E)(\omega M_{13})^2 - 2j\omega^3 M_{12}M_{23}M_{13}]/Z_3$, according to (3), the input-to-output voltage gain can be obtained as follows:

$$G_v(\omega) = \frac{V_o}{V_{\rm in}} = \frac{\frac{\pi}{4}V_{s1}}{\frac{\pi}{4}V_{\rm AB1}} = \left|\frac{j\omega\sqrt{L_1L_2}(k_{12} - k_{13}k_{23})}{Z_1 - j\omega L_1 k_{13}^2 + \frac{L_1L_2\Delta}{\omega^2 R_E}}\right|$$
$$= \left|\frac{k_{12} - k_{13}k_{23}}{1 - \frac{\omega_p^2}{\omega^2} - k_{13}^2 - j\frac{L_2\Delta}{\omega^3 R_E}}\right|\sqrt{\frac{L_2}{L_1}} \tag{4}$$

where $\Delta = \omega^4(k_{12}^2 + k_{13}^2 + k_{23}^2 - 2k_{12}k_{13}k_{23} - 1) + \omega^2(\omega_p^2 + \omega_s^2 - k_{23}^2\omega_p^2 - k_{13}^2\omega_s^2) - \omega_p^2\omega_s^2, \omega_p = 1/\sqrt{L_1C_1}$, $\omega_s = 1/\sqrt{L_2C_2}$. When $\Delta = 0$, there are two frequencies at which the voltage gains are load independent, i.e., (5) and (6), shown at the bottom of this page.

The corresponding load-independent gains are

$$G_v(\omega_L) = \left|\frac{j\omega_L\sqrt{L_1L_2}(k_{12} - k_{13}k_{23})}{Z_1 - j\omega_L L_1 k_{13}^2}\right|$$
$$= \left|\frac{k_{12} - k_{13}k_{23}}{1 - k_{13}^2 - \frac{\omega_p^2}{\omega_L^2}}\right|\sqrt{\frac{L_2}{L_1}} \tag{7}$$

$$G_v(\omega_H) = \left|\frac{j\omega_H\sqrt{L_1L_2}(k_{12} - k_{13}k_{23})}{Z_1 - j\omega_H L_1 k_{13}^2}\right|$$
$$= \left|\frac{k_{12} - k_{13}k_{23}}{1 - k_{13}^2 - \frac{\omega_p^2}{\omega_H^2}}\right|\sqrt{\frac{L_2}{L_1}}. \tag{8}$$

$$\omega_L = \sqrt{\frac{\omega_p^2 + \omega_s^2 - k_{23}^2\omega_p^2 - k_{13}^2\omega_s^2 - \sqrt{(\omega_p^2 + \omega_s^2 - k_{23}^2\omega_p^2 - k_{13}^2\omega_s^2)^2 - 4(1 - k_{12}^2 - k_{23}^2 - k_{13}^2 + 2k_{12}k_{13}k_{23})\omega_p^2\omega_s^2}}{2(1 - k_{12}^2 - k_{23}^2 - k_{13}^2 + 2k_{12}k_{13}k_{23})}} \tag{5}$$

$$\omega_H = \sqrt{\frac{\omega_p^2 + \omega_s^2 - k_{23}^2\omega_p^2 - k_{13}^2\omega_s^2 + \sqrt{(\omega_p^2 + \omega_s^2 - k_{23}^2\omega_p^2 - k_{13}^2\omega_s^2)^2 - 4(1 - k_{12}^2 - k_{23}^2 - k_{13}^2 + 2k_{12}k_{13}k_{23})\omega_p^2\omega_s^2}}{2(1 - k_{12}^2 - k_{23}^2 - k_{13}^2 + 2k_{12}k_{13}k_{23})}} \tag{6}$$

Obviously, the input-output voltage gain is load independent, but is related to the coupling coefficients of MICT. According to (3), the input impedance can be expressed as follows:

$$Z_{\text{in}}(\omega)=\frac{\dot{V}_{\text{AB1}}}{\dot{I}_1}=\frac{Z_1(Z_2+R_E)+(\omega M_{12})^2}{(Z_2+R_E)+(\omega M_{23})^2/Z_3}+\frac{[Z_1(\omega M_{23})^2+(Z_2+R_E)(\omega M_{13})^2-2j\omega^3 M_{12}M_{23}M_{13}]/Z_3}{(Z_2+R_E)+(\omega M_{23})^2/Z_3}. \tag{9}$$

The currents of integrated current sensing winding and primary winding can be solved from the equation set (2) as follows:

$$\dot{I}_1=\frac{-k_{23}^2+\frac{(Z_2+R_E)}{j\omega L_2}}{k_{12}-k_{13}k_{23}}\sqrt{\frac{L_2}{L_1}}\dot{I}_2 \tag{10}$$

$$\dot{I}_3=\frac{k_{12}k_{23}-k_{13}\frac{(Z_2+R_E)}{j\omega L_2}}{k_{12}-k_{13}k_{23}}\sqrt{\frac{L_2}{L_3}}\dot{I}_2. \tag{11}$$

C. Effectiveness of the Self-Oscillating Control Strategy

1) Transfer Impedance: In reference [19], it has been pointed out that the SS-type SOCRC operates at the load-independent frequency when i_2 is either in phase or 180° out of phase with v_{AB1}. But this characteristic is uncertain for the proposed MICT. To facilitate the analysis, we let $h=\omega_s/\omega_p$, and (5) and (6) are then converted to (12) and (13), shown at the bottom of the page.

Then, we have

$$G_v(\omega_L)=\left|\frac{(k_{12}-k_{13}k_{23})f_1(h,k_{12},k_{13},k_{23})^2}{(1-k_{13}^2)f_1(h,k_{12},k_{13},k_{23})^2-1}\right|\sqrt{\frac{L_2}{L_1}} \tag{14}$$

$$G_v(\omega_H)=\left|\frac{(k_{12}-k_{13}k_{23})f_2(h,k_{12},k_{13},k_{23})^2}{(1-k_{13}^2)f_2(h,k_{12},k_{13},k_{23})^2-1}\right|\sqrt{\frac{L_2}{L_1}} \tag{15}$$

where Eqn(16)–(17) shown at the bottom of this page.

According to (3), the transfer impedance can be obtained as follows, in which the definition of Δ is the same as in (4)

$$Z_{21}=\frac{\dot{V}_{\text{AB1}}}{\dot{I}_2}=\frac{\left(\omega L_1-\frac{1}{\omega C_1}-\omega L_1k_{13}^2\right)R_E-j\frac{L_1L_2\Delta}{\omega^2}}{\omega\sqrt{L_1L_2}(k_{12}-k_{13}k_{23})}. \tag{18}$$

Substituting load-independent frequencies ω_L and ω_H into (18), we get

$$Z_{21}(\omega_L)=\frac{R_EL_1(1-k_{13}^2-1/f_1(h,k_{12},k_{13},k_{23})^2)}{\sqrt{L_1L_2}(k_{12}-k_{13}k_{23})} \tag{19}$$

$$Z_{21}(\omega_H)=\frac{R_EL_1(1-k_{13}^2-1/f_2(h,k_{12},k_{13},k_{23})^2)}{\sqrt{L_1L_2}(k_{12}-k_{13}k_{23})}. \tag{20}$$

Since we want to reduce the coupling between the primary winding and the current sensing winding, we have $k_{13}<k_{12}$ for the MICT. Combining $k_{13}<k_{12}$ with $k_{23}<1$ yields

$$k_{12}-k_{13}k_{23}>0. \tag{21}$$

From (21) and (22), shown at the bottom of the next page, we can conclude that $\text{Re}[Z_{21}]<0$ and $\text{Im}[Z_{21}]=0$ at ω_L, $\text{Re}[Z_{21}]>0$ and $\text{Im}[Z_{21}]=0$ at ω_H. In other words, i_2 is lagging v_{AB1} by 180° at ω_L and i_2 is in phase with v_{AB1} at ω_H.

Obviously, i_2 is either in phase or 180° out of phase with v_{AB1} at the load-independent voltage gain for SOCRC with MICT. Next, we will examine whether the converter can operate at the load-independent voltage gain when i_2 and v_{AB1} are in phase.

Assuming i_2 and v_{AB1} are in phase, according to (18), we get

$$\frac{\Delta}{\omega^2C_1C_2}=0,\left(\omega L_1-\frac{1}{\omega C_1}-\omega L_1k_{13}^2\right)R_E>0. \tag{23}$$

Obviously, the load-independent frequency ω_H in (13) is the solution of (23). That means the converter with proposed MICT will operate at the load-independent voltage gain automatically. Likewise, the circuit will operate at ω_L when i_2 is lagging v_{AB1} by 180°.

$$\omega_L=\omega_p\sqrt{\frac{1+h^2-k_{23}^2-h^2k_{13}^2-\sqrt{(1+h^2-k_{23}^2-h^2k_{13}^2)^2-4h^2(1-k_{12}^2-k_{23}^2-k_{13}^2+2k_{12}k_{13}k_{23})}}{2(1-k_{12}^2-k_{23}^2-k_{13}^2+2k_{12}k_{13}k_{23})}} \tag{12}$$

$$\omega_H=\omega_p\sqrt{\frac{1+h^2-k_{23}^2-h^2k_{13}^2+\sqrt{(1+h^2-k_{23}^2-h^2k_{13}^2)^2-4h^2(1-k_{12}^2-k_{23}^2-k_{13}^2+2k_{12}k_{13}k_{23})}}{2(1-k_{12}^2-k_{23}^2-k_{13}^2+2k_{12}k_{13}k_{23})}} \tag{13}$$

$$f_1(h,k_{12},k_{13},k_{23})=\sqrt{\frac{1+h^2-k_{23}^2-h^2k_{13}^2}{2(1-k_{12}^2-k_{23}^2-k_{13}^2+2k_{12}k_{13}k_{23})}-\frac{\sqrt{(1+h^2-k_{23}^2-h^2k_{13}^2)^2-4h^2(1-k_{12}^2-k_{23}^2-k_{13}^2+2k_{12}k_{13}k_{23})}}{2(1-k_{12}^2-k_{23}^2-k_{13}^2+2k_{12}k_{13}k_{23})}} \tag{16}$$

$$f_2(h,k_{12},k_{13},k_{23})=\sqrt{\frac{1+h^2-k_{23}^2-h^2k_{13}^2}{2(1-k_{12}^2-k_{23}^2-k_{13}^2+2k_{12}k_{13}k_{23})}+\frac{\sqrt{(1+h^2-k_{23}^2-h^2k_{13}^2)^2-4h^2(1-k_{12}^2-k_{23}^2-k_{13}^2+2k_{12}k_{13}k_{23})}}{2(1-k_{12}^2-k_{23}^2-k_{13}^2+2k_{12}k_{13}k_{23})}} \tag{17}$$

2) Selection of Operating Point: To realize ZVS, the converter should work in the inductive region. Substituting (12) and (13) into (9), we get

$$\begin{aligned} Z_{\text{in}}(\omega_L) &= \frac{j\omega_L L_1(1-k_{13}^2-1/f_1(h,k_{12},k_{13},k_{23})^2)R_E}{R_E+j\omega_L L_2(1-k_{23}^2-1/f_1(h,k_{12},k_{13},k_{23})^2)} \\ &= \frac{R_E\omega_L^2 L_1L_2[(1-k_{23}^2-1/f_1(h,k_{12},k_{13},k_{23})^2)]^2}{R_E^2+[\omega_L L_2(1-k_{23}^2-1/f_1(h,k_{12},k_{13},k_{23})^2)]^2} \\ &\quad + \frac{jR_E^2\omega_L L_1(1-k_{13}^2-1/f_1(h,k_{12},k_{13},k_{23})^2)}{R_E^2+[\omega_L L_2(1-k_{23}^2-1/f_1(h,k_{12},k_{13},k_{23})^2)]^2} \end{aligned} \tag{24}$$

$$\begin{aligned} Z_{\text{in}}(\omega_H) &= \frac{j\omega_H L_p(1-k_{13}^2-1/f_2(1,k_{12},k_{13},k_{23})^2)R_E}{R_E+j\omega_H L_s(1-k_{23}^2-1/f_2(1,k_{12},k_{13},k_{23})^2)} \\ &= \frac{R_E\omega_H^2 L_1L_2[(1-k_{23}^2-1/f_2(h,k_{12},k_{13},k_{23})^2)]^2}{R_E^2+[\omega_H L_2(1-k_{23}^2-1/f_2(h,k_{12},k_{13},k_{23})^2)]^2} \\ &\quad + \frac{jR_E^2\omega_H L_1(1-k_{13}^2-1/f_2(h,k_{12},k_{13},k_{23})^2)}{R_E^2+[\omega_H L_2(1-k_{23}^2-1/f_2(h,k_{12},k_{13},k_{23})^2)]^2}. \end{aligned} \tag{25}$$

Using (24) and (25), we obtain $\text{Im}[\text{Z}_{\text{in}}]<0$ at ω_L and $\text{Im}[\text{Z}_{\text{in}}]>0$ at ω_H. Thus, the input impedance of the converter is inductive at ω_H, and capacitive at ω_L. Hence, ω_H is chosen as the operating frequency for self-oscillating control strategy.

III. Effects of the Integrated Current Sensing Winding

As shown in (14) and (15), $G_v(\omega_L)$ and $G_v(\omega_H)$, for the SOCRC with the proposed MICT, are dependent on the coupling coefficients between different windings, which are sensitive to the clearances and misalignments. In order to reduce the variations of $G_v(\omega_L)$ and $G_v(\omega_H)$, the constraint conditions of k_{13} and k_{23} are analyzed in this section. Furthermore, due to the interference of the primary winding, the converter will not operate at the voltage gain intersection exactly. The deviation of the operation point and the effect on G_v will be discussed.

A. Load Independent $G_v(\omega)$

For the purpose of simplification, we define g_1 and g_2 as follows:

$$\begin{aligned} g_1(h,k_{12},k_{13},k_{23}) &= G_v(\omega_L)\sqrt{\frac{L_1}{L_2}} \\ &= \left|\frac{(k_{12}-k_{13}k_{23})f_1(h,k_{12},k_{13},k_{23})^2}{(1-k_{13}^2)f_1(h,k_{12},k_{13},k_{23})^2-1}\right| \\ &= \left|\frac{1-h^2-k_{23}^2+h^2k_{13}^2}{2(k_{12}-k_{13}k_{23})}-\sqrt{\left[\frac{1-h^2-k_{23}^2+h^2k_{13}^2}{2(k_{12}-k_{13}k_{23})}\right]^2+h^2}\right| \end{aligned} \tag{26}$$

$$\begin{aligned} g_2(h,k_{12},k_{13},k_{23}) &= G_v(\omega_H)\sqrt{\frac{L_1}{L_2}} \\ &= \left|\frac{(k_{12}-k_{13}k_{23})f_2(h,k_{12},k_{13},k_{23})^2}{(1-k_{13}^2)f_2(h,k_{12},k_{13},k_{23})^2-1}\right| \\ &= \left|\frac{1-h^2-k_{23}^2+h^2k_{13}^2}{2(k_{12}-k_{13}k_{23})}+\sqrt{\left[\frac{1-h^2-k_{23}^2+h^2k_{13}^2}{2(k_{12}-k_{13}k_{23})}\right]^2+h^2}\right|. \end{aligned} \tag{27}$$

Obviously, $G_v(\omega_L)$ and $G_v(\omega_H)$ will tend to be constant for different extents of clearances and misalignments when the following is satisfied:

$$\frac{1-h^2-k_{23}^2+h^2k_{13}^2}{2(k_{12}-k_{13}k_{23})} << h. \tag{28}$$

When clearances or misalignments change, k_{12} and k_{23} will vary accordingly, while h and k_{13} will remain unchanged. Since $k_{12}<1, k_{12}>>k_{13}k_{23}$, the numerator in the left side of (28)

$$\begin{aligned} &\because \left(h^2+k_{23}^2-h^2k_{13}^2-1\right)^2-[(1+h^2-k_{23}^2-h^2k_{13}^2)^2-4h^2(1-k_{12}^2-k_{23}^2-k_{13}^2+2k_{12}k_{13}k_{23})] \\ &\quad = [(h^2+k_{23}^2-h^2k_{13}^2-1)-\sqrt{(1+h^2-k_{23}^2-h^2k_{13}^2)^2-4h^2(1-k_{12}^2-k_{23}^2-k_{13}^2+2k_{12}k_{13}k_{23})}] \\ &\qquad \cdot [(h^2+k_{23}^2-h^2k_{13}^2-1)+\sqrt{(1+h^2-k_{23}^2-h^2k_{13}^2)^2-4h^2(1-k_{12}^2-k_{23}^2-k_{13}^2+2k_{12}k_{13}k_{23})}] \\ &\quad = -4h^2(k_{12}-k_{23}k_{13})^2<0 \\ &\therefore 1-k_{13}^2-1/f_1(h,k_{12},k_{13},k_{23})^2 \\ &\quad = \frac{(h^2+k_{23}^2-h^2k_{13}^2-1)-\sqrt{(1+h^2-k_{23}^2-h^2k_{13}^2)^2-4h^2(1-k_{12}^2-k_{23}^2-k_{13}^2+2k_{12}k_{13}k_{23})}}{2h^2}<0 \\ &\therefore 1-k_{13}^2-1/f_2(h,k_{12},k_{13},k_{23})^2 \\ &\quad = \frac{(h^2+k_{23}^2-h^2k_{13}^2-1)+\sqrt{(1+h^2-k_{23}^2-h^2k_{13}^2)^2-4h^2(1-k_{12}^2-k_{23}^2-k_{13}^2+2k_{12}k_{13}k_{23})}}{2h^2}>0 \end{aligned} \tag{22}$$

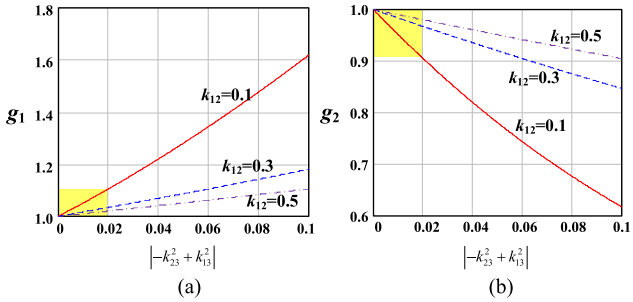

Fig. 5. Relationship between (a) g_1, (b) g_2 and $|-k_{23}^2+k_{13}^2|$.

should tend to zero. It can be shown that (28) is satisfied if h, k_{13}, and k_{23} satisfy

$$\text{if}\begin{cases} h\approx 1 \\ k_{23}\approx 0 \\ k_{13}\approx 0 \end{cases}\text{ or }\begin{cases} h=1 \\ k_{23}=k_{13} \end{cases},\ 1-k_{23}^2\approx h^2\left(1-k_{13}^2\right). \quad (29)$$

Since k_{23} changes with air gaps and k_{13} remains constant, (29) can be satisfied. Next, we will discuss the ranges of k_{13} and k_{23}.

Given $h=1$, we have k_{13} and k_{23} leading to zero. Equations (26) and (27) can be written as

$$g_1(h,k_{12},k_{13},k_{23})\approx\left|\frac{-k_{23}^2+k_{13}^2}{2k_{12}}-\sqrt{\left[\frac{-k_{23}^2+k_{13}^2}{2k_{12}}\right]^2+1}\right| \quad (30)$$

$$g_2(h,k_{12},k_{13},k_{23})\approx\left|\frac{-k_{23}^2+k_{13}^2}{2k_{12}}+\sqrt{\left[\frac{-k_{23}^2+k_{13}^2}{2k_{12}}\right]^2+1}\right|. \quad (31)$$

According to the above equations, the curve of g_1, g_2 versus $|-k_{23}^2+k_{13}^2|$ can be drawn for different values of k_{12}, as shown in Fig. 5.

It can be shown that the variation rates of g_1 and g_2 are both less than 10% if $|-k_{23}^2+k_{13}^2|$ satisfies

$$\left|-k_{23}^2+k_{13}^2\right|<0.02. \quad (32)$$

The above inequality can be used as a constraint condition for the SS-type SOCRC with MCIT. Satisfying this inequality implies that the variation rates of $G_v(\omega_L)$ and $G_v(\omega_H)$ defined by (26) and (27) are both less than 10%.

B. Operation Point Deviation and Its Effect on $G_v(\omega)$

The above discussion on $G_v(\omega)$ assumes that i_2 is always in phase or 180° out of phase with v_{AB}. However, in practice, the switching frequency will deviate from the load-independent point.

As mentioned in Section II-A, the phase difference between i_2 and v_{AB} is caused by the practical operation of the MICT and other functional blocks. For the MICT, the phase angle of I_3/I_2, denoted as θ_1, is affected by the primary current due to the existence of k_{13}. From the measured results, the time delay t_d caused by other functional blocks is nearly constant. In order to

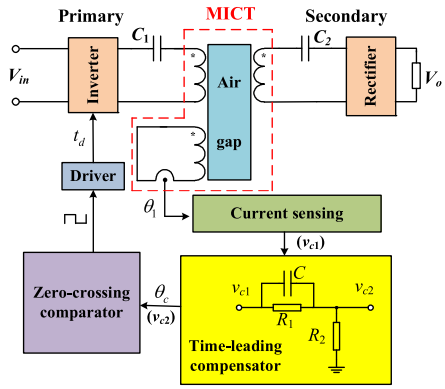

Fig. 6. Control diagram with time-leading block.

eliminate this phase detection error, a time-leading compensator has been proposed in [19], as shown in Fig. 6. Also, v_{c1} is the output signal of the comparator and v_{c2} is the output signal of the time-leading compensator. The phase leading angle caused by the compensator can be described as follows:

$$\theta_c=\arctan\left(\omega R_1C\right)-\arctan\left(\frac{\omega R_1R_2C}{R_1+R_2}\right). \quad (33)$$

Thus, the phase angle of the transfer impedance θ can finally be simplified as

$$\theta=\theta_1+\theta_c-t_d\times\omega. \quad (34)$$

1) Phase Angle of I_3/I_2: Equation (11) can be further delineated as follows:

$$\frac{\dot{I}_3}{\dot{I}_2}=\frac{k_{12}k_{23}-k_{13}\left(1-\frac{\omega_s^2}{\omega^2}-j\frac{R_E}{\omega L_2}\right)}{k_{12}-k_{13}k_{23}}\sqrt{\frac{L_2}{L_3}}. \quad (35)$$

Obviously, i_3 is in phase with i_2 when $k_{13}=0$. But in practical applications, the phase angle of I_3/I_2 will vary with different clearances and load conditions. So, the phase angle of I_3/I_2 can be delineated as follows:

$$\theta_1=\arctan\left(\frac{\frac{R_E}{\omega L_2}}{\frac{k_{23}k_{12}}{k_{13}}-\left(1-\frac{\omega_s^2}{\omega^2}\right)}\right). \quad (36)$$

From (33), (34), and (36), it is readily seen that as the load increases, R_E will decrease and so will θ_1 and θ, when the coupling coefficients of the MICT are unchanged.

According to the discussion of Section II, $v_{\mathrm{AB}1}$ is in phase with i_2 when $\omega=\omega_H$. Ignoring the time delay of other control blocks, θ_1 tends to zero. Consequently, we have $\mathrm{Re}[I_3/I_2]>0$. Considering $0<(\omega_s/\omega_H)^2<1$, it can be found that $\mathrm{Re}[I_3/I_2]>0$ if k_{13} satisfies

$$k_{13}<k_{12}k_{23}. \quad (37)$$

Substituting (37) into (32), the solution of k_{23} is given as

$$k_{23}<\sqrt{\frac{0.02}{1-k_{12}^2}}. \quad (38)$$

It is obvious that the smaller the k_{12}, the smaller k_{23} and k_{13}. Considering the extreme case of $k_{12}=0$, k_{23} should be less

than 0.141, and (37) and (38) will become

$$\begin{cases} k_{23} < 0.141 \\ k_{13} < 0.141 k_{12}. \end{cases} \tag{39}$$

2) Characteristics at Practical Operating Point: Substituting (33) and (36) into (34), the phase angle of the transfer impendence can be written as

$$\theta = \arctan\left(\frac{\frac{R_E}{\omega L_2}}{\frac{k_{23}k_{12}}{k_{13}} - \left(1 - \frac{\omega_s^2}{\omega^2}\right)}\right) + \arctan(\omega R_1 C) - \arctan\left(\frac{\omega R_1 R_2 C}{R_1 + R_2}\right) - t_d \times \omega. \tag{40}$$

The relationship between θ and ω can be derived from (15), i.e., (41) as shown at the bottom of this page.

From this equation, we readily get $f'_\theta(\omega) > 0$ when $\omega > \omega_p$. Obviously, $f_\theta(\omega)$ is a monotonic increasing function when ω is near ω_H. At this operating point, $\tan\theta$ is approximately equal to θ, and the relationship between $\Delta\omega$ and θ can be easily derived as

$$\Delta\omega = \omega - \omega_H \approx \frac{f_\theta(\omega) - f_\theta(\omega_H)}{f'_\theta(\omega)\,|_{\omega=\omega_H}} = \frac{\theta}{f'_\theta(\omega)\,|_{\omega=\omega_H}}. \tag{42}$$

Substituting (40) into (4) yields

$$G_v(\omega+\Delta\omega)\,|_{\omega=\omega_H} = \sqrt{\frac{L_2}{L_1}}\left|\frac{(k_{12} - k_{13}k_{23})}{\left(1 - \frac{\omega_p^2}{(\omega_H+\Delta\omega)^2} - k_{13}^2\right)(1 + jf'_\theta(\omega)\,|_{\omega=\omega_H}\ \Delta\omega)}\right| = \sqrt{\frac{L_2}{L_1}}\left|\frac{(k_{12} - k_{13}k_{23})}{\left(1 - \frac{\omega_p^2}{(\omega_H + \frac{\theta}{f'_\theta(\omega)|_{\omega=\omega_H}})^2} - k_{13}^2\right)(1 + j\theta)}\right|. \tag{43}$$

It can be seen that $G_v(\omega)$ is a monotonic decreasing function with θ around ω_H.

Equation (36) indicates that θ_1 and θ will decrease with the load. From the above analysis, we know that $f_\theta(\omega)$ around ω_H is monotonically increasing, and $G_v(\omega)$ around ω_H is monotonically decreasing. Therefore, increasing the load will lead to a decrease of the operating frequency, which might result in an increase of $G_v(\omega)$.

The numerical results as shown in Fig. 7 are generated from the analytical equations. The MICT parameters for the calculation are listed in Table I, which satisfy the requirement of (39).

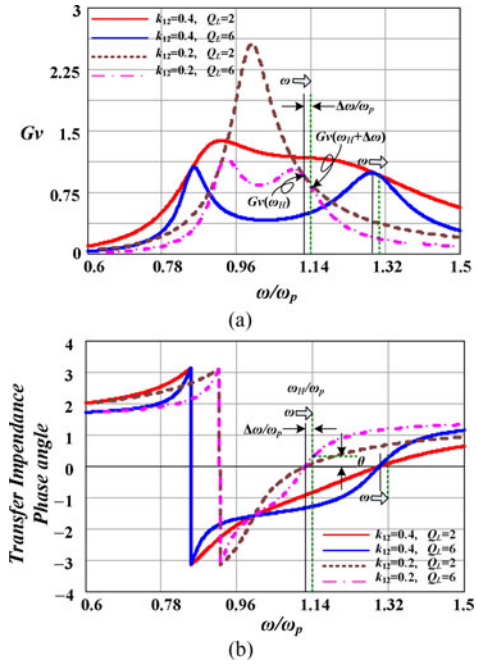

Fig. 7. (a) Plots of input-to-output voltage gain. (b) Plots of phase angle of transfer impedance.

TABLE I
MICT PARAMETERS FOR NUMERICAL CALCULATIONS

k_{12}	k_{13}	k_{23}
0.4	0.028	0.14
0.2	0.028	0.14

Assuming $L_1 = L_2, \omega_p = \omega_s$, substituting the MICT parameters and $Q_L = \omega_p L_2 / R_E$ into (4) and (18), the output voltage gain and the phase angle of the transfer impedance can then be plotted, as shown in Fig. 7.

It can be seen that, consistent with the theoretical analysis, θ increases with ω around ω_H and $G_v(\omega)$ decreases with ω. As indicated in (36), θ will decrease with the load, which leads to the decrease of frequency according to Fig. 7(a). Comparing $G_v(\omega_H, 6)$ and $Gv(\omega_H + \Delta\omega, 2)$ with $k_{12} = 0.4$, as shown in Fig. 7(a), we see that increasing the load might lead to increase of $G_v(\omega)$ due to the lowered frequency.

IV. MICT CONFIGURATIONS

In order to reduce the variations of $G_v(\omega_L)$ and $G_v(\omega_H)$ under different clearances and loads, the design of MICT should

$$\tan\theta = f_\theta(\omega) = \frac{-\frac{L_2\Delta}{\omega^2 R_E}}{\omega\left(1 - \frac{1}{\omega^2 L_1 C_1} - k_{13}^2\right)} = \frac{\omega_p L_2}{R_E} \cdot \left(\frac{\left(\frac{\omega}{\omega_p}\right)^4 (1 - \mathrm{k}_{12}^2 - \mathrm{k}_{13}^2 - \mathrm{k}_{23}^2 + 2\mathrm{k}_{12}\mathrm{k}_{13}\mathrm{k}_{23}) - \left(\frac{\omega}{\omega_p}\right)^2 (1 + h^2 - \mathrm{k}_{23}^2 - \mathrm{k}_{13}^2) + h^2}{\frac{\omega}{\omega_p}\left[\left(\frac{\omega}{\omega_p}\right)^2 + k_{13}^2 - 1\right]}\right) \tag{41}$$

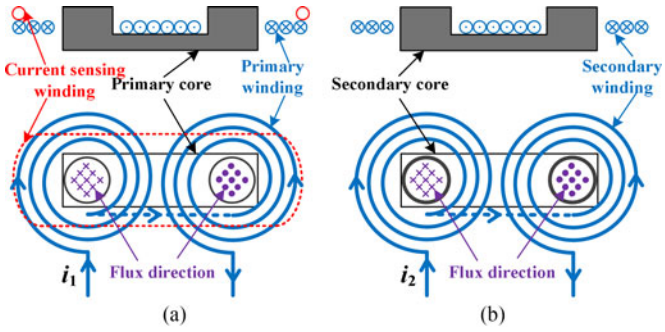

Fig. 8. One type of proposed MICT. (a) Primary part. (b) Secondary part.

satisfy (39). Besides, it is better to get an MICT structure with large coupling coefficient k_{12} leading to higher efficiency.

In order to obtain larger k_{12}, smaller core size, and lighter weight, a planar U-structure magnetic core is used here, which is studied in [26], as shown in Fig. 8.

In order to get a low k_{13} satisfying (39), we can use flux cancellation [27] since the magnetic circuit of the primary winding and current sensing winding cannot be separated. Fig. 8 shows an example of an MICT structure. It can be seen that the primary winding is split into two windings in series. The integrated current sensing winding is coupled with the two primary windings at the same time. The flux coupled by the current sensing winding is produced by the two primary windings in opposite directions. By adjusting the relative position, the coupling coefficient of current sensing winding and primary winding can be made to approach zero.

Previous studies [21] have shown that the "DD" winding structure can increase the coupling coefficient. The secondary winding is split into two windings in series, as shown in Fig. 8. Furthermore, the coupling coefficient between the secondary winding and the integrated current sensing winding approaches zero under symmetry, which satisfies the requirement of (39).

The structure shown in Fig. 8 is an example of MICT. Based on the flux cancellation concept, we can derive other solutions of MICT. Fig. 9 gives two examples. Panels (a) and (c) of Fig. 9 are two types of primary parts of an MICT.

The integrated current sensing windings are split into two windings in series. The fluxes coupled by the two current sensing windings are in the opposite directions. Panels (b) and (d) of Fig. 9 are the secondary parts, which use a circular structure. Compared to the structure shown in Fig. 8, these two structures are not better choices because of lower k_{12} and bigger core size.

V. Experimental Results and Discussions

A. Parameters of SOCRC With MICT

An 80-W SS-type SOCRC with MICT having an air gap of 10–30 mm is fabricated to verify the analysis. Detailed specifications are shown in Table II. Based on Table II, the parameters of the components of an SS-type SOCRC with MICT are shown in Table III.

According to the analysis in Section IV, the primary winding is surrounded by the current sensing winding. The secondary winding is split into two serially connected windings, as shown in Fig. 10.

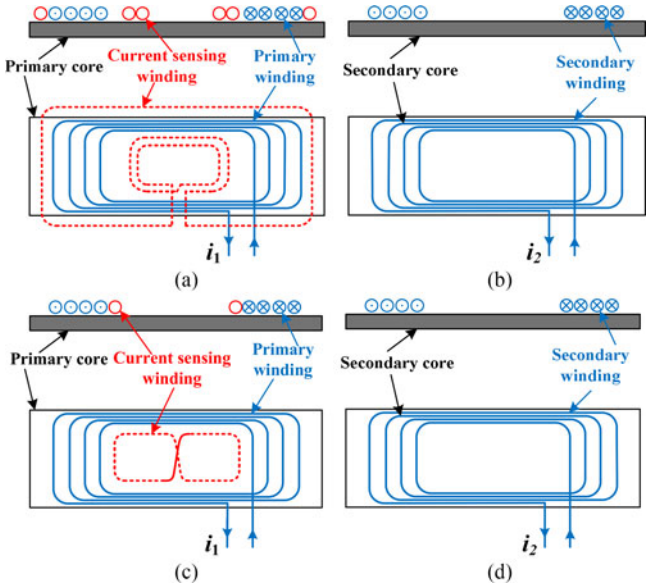

Fig. 9. Other types of MICT configurations. (a) Primary part I. (b) Secondary part I. (c) Primary part II. (d) Secondary part II.

TABLE II
Specification

DC input voltage	30 V
DC output voltage	27 V
Output power	30–80 W
Air gap range	10–30 mm

TABLE III
Parameters of the Components of SS-Type SOCRC With MICT

Inverter MOSFETs	IRFB3307
Rectifier Diodes	B40250TG, $V_F = 0.7$ V
Primary side resonant capacitance C_1	33 nF
Secondary side resonant capacitance C_2	32.4 nF
MICT	3F3, primary/secondary side winding are two winding in series structure, specification see Table. IV.
Time-leading compensator	$R_1 = 4.9\ k, R_2 = 1\ k, C = 125$ pF
Time delay of control blocks	$t_d = 500$ ns

Fig. 11 shows the relationship between k_{12}, k_{23} and the misalignment distance ΔX, with the air gap being 20 mm. Table IV shows the parameters of MICT under different clearance conditions. It can be found that these parameters satisfy the constraint condition of (39).

B. Experimental and Simulation Results of Input-to-Output Voltage Gain

Substituting the parameters of Table IV into (4), the calculated input-to-output voltage gain can be obtained by Mathcad software. In the experiment, the SOCRC works with an external

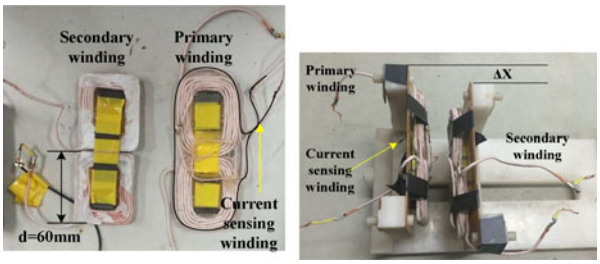

Fig. 10. Photos of the proposed MICT.

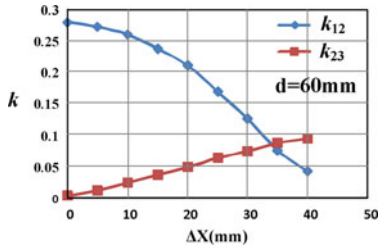

Fig. 11. Relationship between k_{12}, k_{23}, and ΔX at 20 mm air gap.

TABLE IV
TRANSFORMER PARAMETERS UNDER DIFFERENT CLEARANCES

Air gap	L_1/uH	L_2/uH	L_3/uH	h
10 mm	64.1	64.9	1.57	1.003
20 mm	57.7	58.3	1.54	1.004
30 mm	56.5	57.3	1.49	1.002
Air gap	k_{12}	k_{13}	k_{23}	
10 mm	0.3925	0.007	0.042	
20 mm	0.2390	0.002	0.029	
30 mm	0.1507	0.0003	0.023	

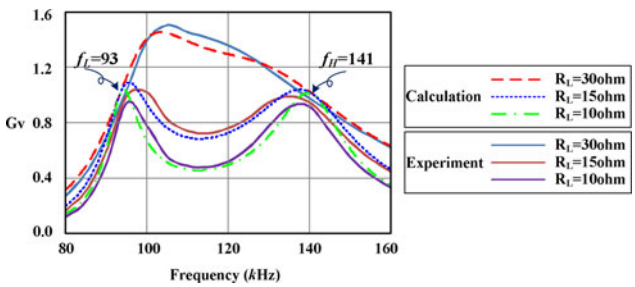

Fig. 12. Plots of G_v for different loads with 10 mm air gap.

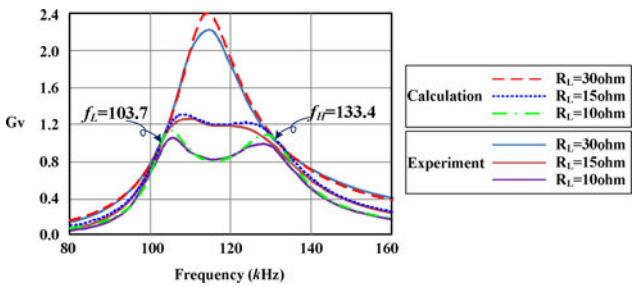

Fig. 13. Plots of G_v for different loads with 20 mm air gap.

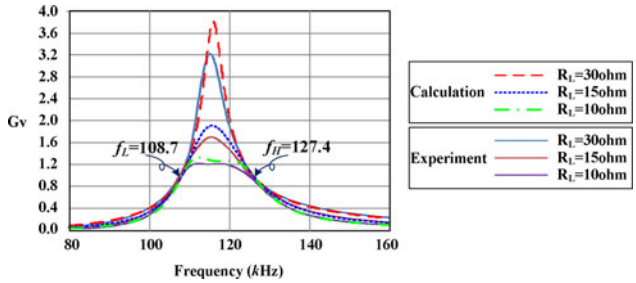

Fig. 14. Plots of G_v for different loads with 30 mm air gap.

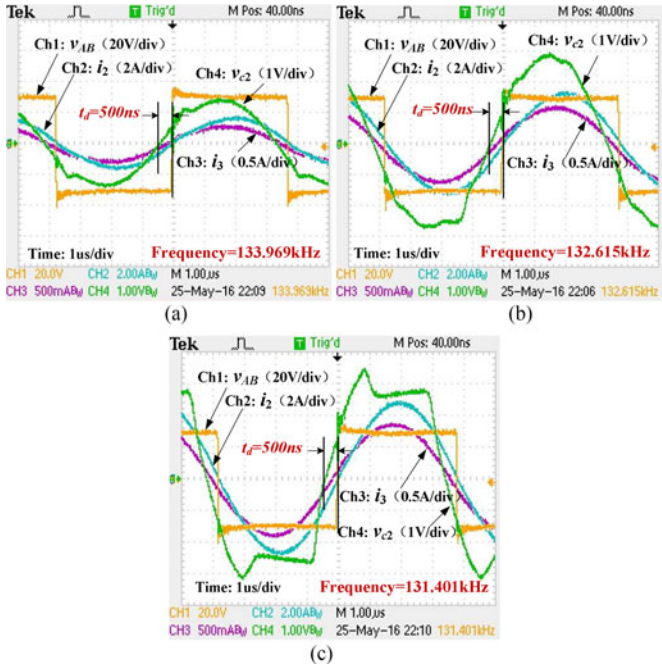

Fig. 15. Waveforms of i_2, i_3, $v_{\rm AB}$, and v_{c2} for different loads with an air gap of 20 mm. (a) $I_o = 1.2$A. (b) $I_o = 2$A. (c) $I_o = 3$A.

drive signal. Figs. 12–14 show the calculated results and the corresponding experimental results. It can be seen that the calculated and the measured results are very close. The difference is caused by the resistance of devices and windings.

C. Steady-State Waveforms

Fig. 15 gives the steady-state waveforms under different values of the load with an air gap of about 20 mm, illustrating the operation of the self-oscillating control. Here, v_{c2} is the output signal of the lead compensator, as shown in Fig. 6. It can be seen that the zero-crossing-point time delay t_d between v_{c2} and $v_{\rm AB}$ is almost constant. As shown in Fig. 15, the fundamental component of the inverter's output voltage $v_{\rm AB}$ and the secondary current i_2 are in phase. Moreover, the switching frequency decreases with increasing load, which is consistent with the theoretical analysis.

Fig. 16 gives the steady-state waveforms under different clearances when $I_o = 2$ A. The switching frequency is 141.496, 132.674, and 126.807 kHz when air gap = 10, 20, and 30 mm, respectively. According to the calculation flow chart shown in

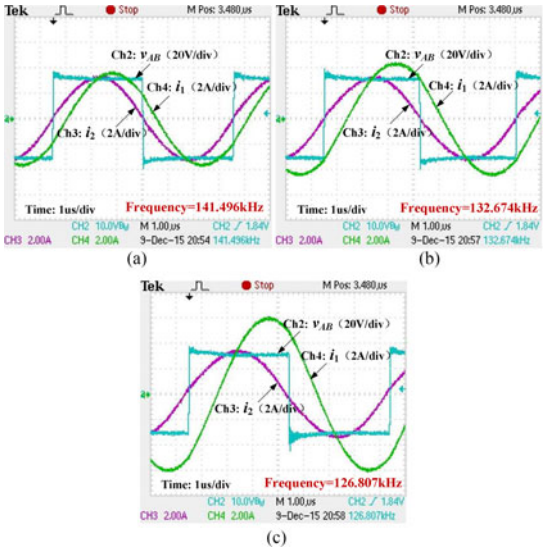

Fig. 16. Waveforms of i_1, i_2, and v_{AB} under different clearances when $I_o = 2\mathrm{A}$. (a) Air gap = 10 mm. (b) Air gap = 20 mm. (c) Air gap = 30 mm.

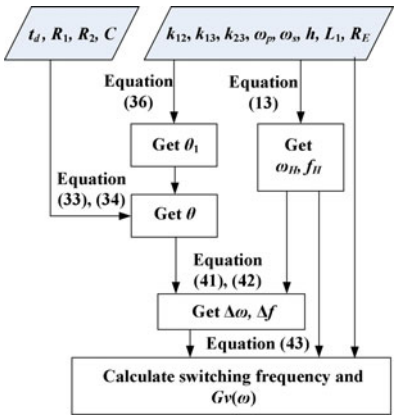

Fig. 17. Calculation flow chart.

TABLE V
CALCULATED AND EXPERIMENTAL FREQUENCY UNDER DIFFERENT CLEARANCES

Air gap (mm)	R_E (ohm)	f_H (kHz)	θ	Δf (kHz)	Calculated frequency (kHz)	Measured frequency (kHz)
10	10.94	141.1	–0.028	–0.322	140.8	141.496
20	10.94	133.4	–0.045	–0.5	132.9	132.674
30	10.94	127.4	–0.079	–0.83	126.5	126.807

TABLE VI
CALCULATED AND EXPERIMENTAL FREQUENCY UNDER DIFFERENT LOAD CONDITIONS

I_o (A)	R_E (ohm)	f_H (kHz)	θ	Δf (kHz)	Calculated frequency (kHz)	Measured frequency (kHz)
1.2	21.88	133.4	0.016	0.029	133.4	133.526
2	10.94	133.4	–0.045	–0.5	132.9	132.674
3	7.3	133.4	–0.068	–0.51	132.9	131.967

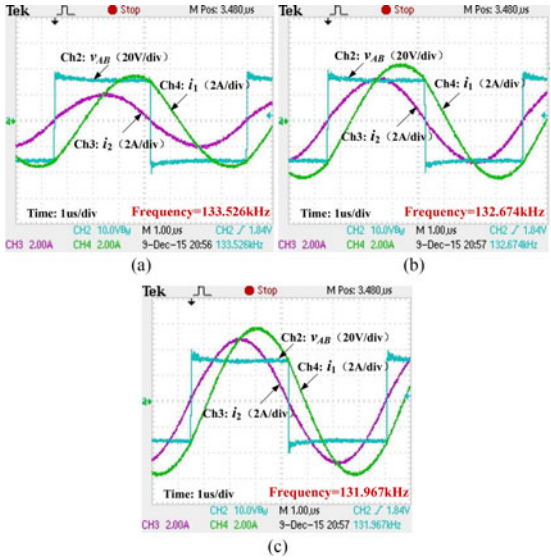

Fig. 18. Waveforms of i_1, i_2, and v_{AB} for different loads at 20 mm air gap. (a) $I_o = 1.2\mathrm{A}$. (b) $I_o = 2\mathrm{A}$. (c) $I_o = 3\mathrm{A}$.

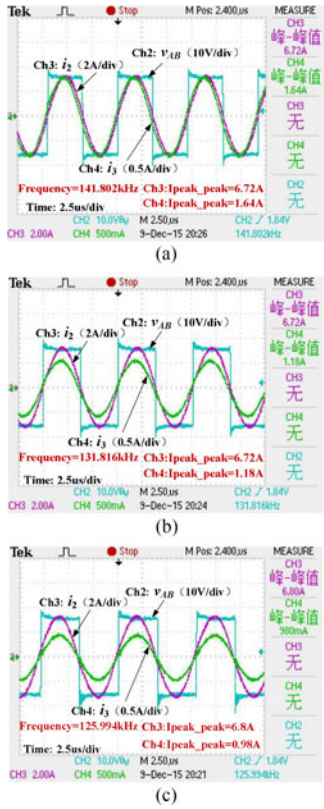

Fig. 19. Waveforms of i_2, i_3, and v_{AB} under different clearances when $I_o = 2\mathrm{A}$. (a) Air gap = 10 mm. (b) Air gap = 20 mm. (c) Air gap = 30 mm.

Fig. 17, the working frequency can be calculated with the help of Mathcad software. As shown in Table V, the numerical results are very close to the experimental results.

Substituting the known parameters into the calculation flow chart, a similar set of results can be obtained, as shown in Table VI and Fig. 18. It is observed that the calculations are very close to the experimental results.

TABLE VII
CALCULATED AND EXPERIMENTAL VALUE OF $|I_3/I_2|$ UNDER DIFFERENT CLEARANCES

Air Gap (mm)	$\lvert I_3/I_2\rvert$ Calculated value	$\lvert I_3/I_2\rvert$ Experimental value
10 mm	0.233	0.244
20 mm	0.17	0.175
30 mm	0.141	0.144

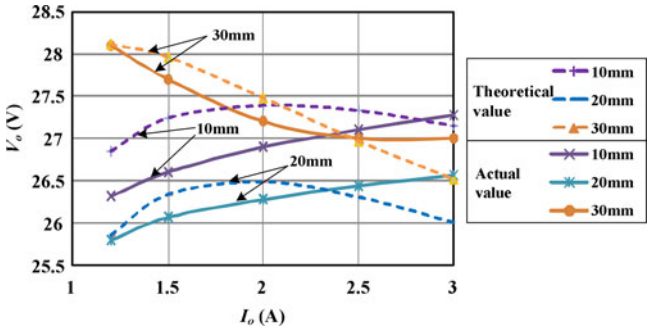

Fig. 20. Theoretical and actual output voltage at different clearances.

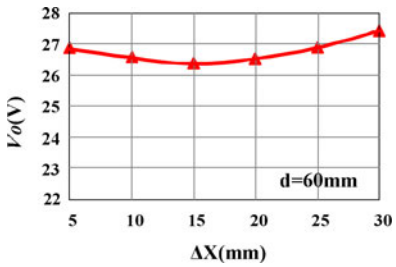

Fig. 21. Output voltage under misalignments with 20 mm air gap and $I_o = 2$A.

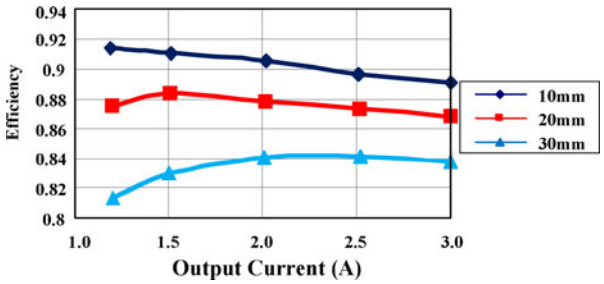

Fig. 22. Efficiency versus I_o.

Fig. 19 shows the waveforms of i_2 and i_3 when air gap = 10, 20, and 30 mm and $I_o = 2$ A. The peak-to-peak value of i_2 and i_3 can be found in the figure. Substituting the parameters of Table IV into (35), the value of $|I_3/I_2|$ can be calculated. Table VII shows the calculated and experimental values of $|I_3/I_2|$. The calculations match the experimental results well, verifying the previous analysis.

D. Load Regulation and Converter Efficiency

1) Load Regulation: Fig. 17 shows the calculation procedure to get the theoretical voltage gain $Gv(\omega_H)_{\_\mathrm{cal}}$. In order

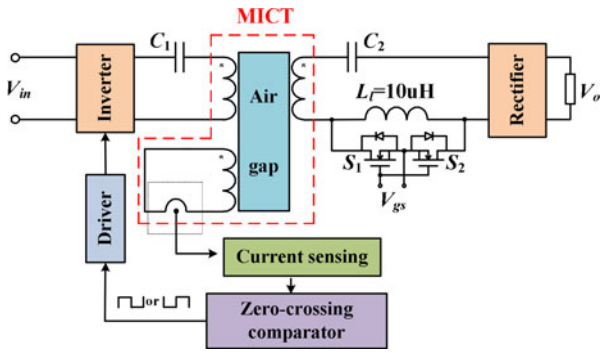

Fig. 23. Circuit for testing dynamic performance.

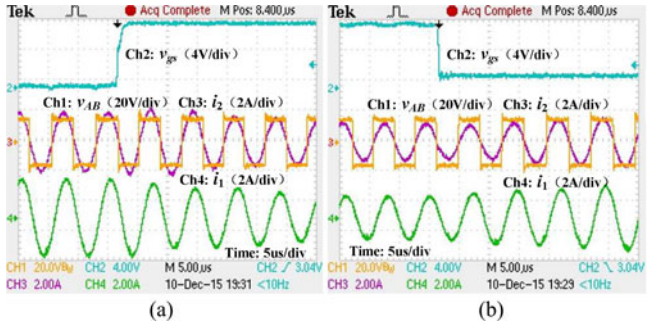

Fig. 24. Dynamic experimental waveforms. (a) Switch out L_l. (b) Switch in L_l.

to facilitate comparison, the primary winding resistor is set as $R_p = 0.15$, the secondary winding resistor $R_s = 0.15$, and the forward voltage of rectifier diodes V_F should be introduced. The calculated voltage can be found as

$$V_o = \frac{V_{\mathrm{IN}} R_E G_v(\omega_H)_{\_\mathrm{cal}}}{\left| R_s + R_E + R_p G_v(\omega_H)_{\_\mathrm{cal}} \left(\frac{(Z_2 + R_E)}{j\omega M_{12}} + \frac{k_{23}^2}{k_{12}} \right) \right|} - 2V_F. \tag{44}$$

Substituting the value of R_p, R_s, and V_F to the above-mentioned equation, the theoretical output voltage can be obtained. Fig. 20 shows the calculated and measured output voltage curves. It can be observed that the theoretical value is very close to the actual value. In addition, the output voltage at 10 or 20 mm air gap increases with the load. This matches the analytical result of Section III.

2) Output Voltage Under Misalignment Condition: Fig. 21 shows the relationship between the output voltage and ΔX when the air gap is 20 mm and $I_o = 2$ A. It is an example of misalignment. The output voltage changes slightly with ΔX. The change of ΔX just leads to the changes of k_{12} and k_{23}, as shown in Fig. 11. It is very similar to the case of varying clearance.

3) Efficiency: Fig. 22 shows the measured efficiency from the dc input to the dc output of the converter. A relatively high efficiency has been achieved, e.g., 91.5% for 10-mm gap, and 88.5% for 20-mm gap.

E. Dynamic Performance

To verify the dynamic performance of SOCRC with MICT, a test circuit, which is similar to that given in [19], is built to emulate the parameter changes, as shown in Fig. 23. Here, L_l (10 μH)is added to emulate the change in the leakage inductance. As shown in Fig. 24, when L_l is switched in or out of the circuit, the operating frequency can change to the new self-oscillating operating frequency in a switching period.

VI. Conclusion

This paper proposes a multifunction contactless transformer, which integrates the functions of power transfer and passive current phase detection in an SOCRC. The operating characteristics of the multifunction contactless transformer in an SS compensated SOCRC are analyzed by using a mutual inductance model. Given the relationship between the coupling coefficient of the primary winding, the current sensing winding, and the voltage gain, it is possible to find two load-independent operating frequencies for this transformer. Considering the requirement of a very small change of voltage gain at load-independent frequency under different clearance and misalignment conditions, two constraint conditions for this integrated transformer are derived. Furthermore, the characteristics of the output voltage at a particular operating point are analyzed in detail. Then, the MICT configurations are given. An 80-W SS SOCRC is built by using the proposed integrated transformer. The experimental results match the analytical results.

References

[1] A. Ramrakhyani, S. Mirabbasi, and M. Chiao, "Design and optimization of resonance-based efficient wireless power delivery systems for biomedical implants," *IEEE Trans. Biomed. Circuits Syst.*, vol. 5, no. 1, pp. 48–63, Feb. 2011.

[2] G. A. Covic and J. T. Boys, "Inductive power transfer," *Proc. IEEE*, vol. 101, no. 6, pp. 1276–1289, Jun. 2013.

[3] G. A. Covic and J. T. Boys, "Modern trends in inductive power transfer for transportation applications," *IEEE J. Emerg. Select. Topics Power Electron.*, vol. 1, no. 1, pp. 28–41, Mar. 2013.

[4] J. S. Ho, S. Kim, and A. S. Y. Poon, "Midfield wireless powering for implantable systems," *Proc. IEEE*, vol. 101, no. 6, pp. 1369–1378, Jun. 2013.

[5] S. Y. R Hui, "Planar wireless charging technology for portable electronic products and qi," *Proc. IEEE*, vol. 101, no. 6, pp. 1290–1301, Jun. 2013.

[6] S. Y. R. Hui, W. Zhong, and C. Lee, "A critical review of recent progress in mid-range wireless power transfer," *IEEE Trans. Power Electron.*, vol. 29, no. 9, pp. 4500–4511, Sep. 2014.

[7] S. Li and C. C. Mi, "Wireless power transfer for electric vehicle applications," *IEEE J. Emerg. Select. Topics Power Electron.*, vol. 3, no. 1, Mar. 2015, Art. no. 4517.

[8] S. Y. R. Hui, W. X. Zhong, and C. K. Lee, "A critical review of recent progress in mid-range wireless power transfer," *IEEE Trans. Power Electron.*, vol. 29, no. 9, pp. 4500–4511, Sep. 2014.

[9] J. Hou, Q. Chen, S. C. Wong, C. K. Tse, and X. Ruan, "Analysis and control of series-series-parallel compensated resonant converter for contactless power transfer," *IEEE J. Emerg. Sel. Topics Power Electron.*, vol. 3, no. 1, pp. 124–136, Mar. 2015.

[10] J. L. Villa, J. Sallan, J. F. Sanz Osorio, and A. Llombart, "High-misalignment tolerant compensation topology for ICPT systems," *IEEE Trans. Ind. Electron.*, vol. 59, no. 2, pp. 945–951, 2012.

[11] S. Ping, A. P. Hu, S. Malpas, and D. Budgett, "A frequency control method for regulating wireless power to implantable devices," *IEEE Trans. Biomed. Circuits Syst.*, vol. 2, no. 1, pp. 22–29, Mar. 2008.

[12] D. Ahn and S. Hong, "Wireless power transmission with self-regulated output voltage for biomedical implant," *IEEE Trans. Ind. Electron.*, vol. 61, no. 5, pp. 2225–2235, May 2014.

[13] Q. Chen, S. C. Wong, C. K. Tse, and X. Ruan, "Analysis, design, and control of a transcutaneous power regulator for artificial hearts," *IEEE Trans. Biomed. Circuits Syst.*, vol. 3, no. 1, pp. 23–31, Feb. 2009.

[14] T.-S. Chan and C.-L. Chen, "A primary side control method for wireless energy transmission system," *IEEE Trans. Circuits Syst. I, Reg. Papers*, vol. 59, no. 8, pp. 1805–1814, Aug. 2012.

[15] J. U. W. Hsu, A. P. Hu, and A. Swain,"A wireless power pickup based on directional tuning control of magnetic amplifier, " *IEEE Trans. Ind. Electron.*, vol. 56, no, 7, pp. 2771–2781, Jul. 2009.

[16] H. L. Li, A. P. Hu, and G. A. Covic, "A power flow control method on primary side for a CPT system," in *Proc. IEEE Int. Power Electron. Conf.*, 2010, pp. 1050–1055.

[17] M. Fu, C. Ma, and X. Zhu, "A cascaded boost-buck converter for high efficiency wireless power transfer systems," *IEEE Trans. Ind. Informat.*, vol. 10, no. 3, pp. 1972–1980, Aug. 2014.

[18] H. Li, J. Li, K. Wang, W. Chen, and X. Yang, "A maximum efficiency point tracking control scheme for wireless power transfer systems using magnetic resonant coupling," *IEEE Trans. Power Electron.*, vol. 30, no. 7, pp. 3998–4008, Jul. 2015.

[19] K. Yan, Q. Chen, J. Hou, W. Chen, X. Ren, and X. Ruan, "Self-oscillating contactless resonant converter with phase detection contactless current transformer," in *Proc. IEEE Energy Conv. Congr. Exp.*, 2013, pp. 2920–2927.

[20] M. K. Kazimierczuk and D. Czarkowski, *Resonant Power Converters*. New York, NY, USA: Wiley, 1995.

[21] M. Budhia, J. T. Boys, G. A. Covic and C-Y. Huang, "Development of a single-sided flux magnetic coupler for electric vehicle IPT charging systems," *IEEE Trans. Ind. Electron.*, vol. 60, no. 1, pp. 318–328, Jan. 2013.

[22] C. M. Zierhofer and E. S. Hochmair, "The class-E concept for efficient wide-band coupling-insensitive transdermal power and data transfer," in *Proc. IEEE 14th Annu. Int. Conf. Eng. Med. Biol. Soc.*, 1992, vol. 2, pp. 382–383.

[23] L. Xu, Q. Chen, X. Ren, S. Ping, and S.-C.Wong, "Self-oscillating contactless resonant converter with power transfer and current sensing integrated transformer," in *Proc. IEEE Energy Conv. Congr. Exp.*, 2015, pp. 4539–4543.

[24] X. Ren, Q. Chen, L. Cao, X. Ruan, S-C. Wong, and C. K. Tse. "Characterization and control of self-oscillating contactless resonant converter with fixed voltage gain," in *Proc. IEEE Int. Power Electron. Motion Control Conf.*, 2012, pp. 1822–1827.

[25] E. Gati, G. Kampitsis, I. Stavropoulos, S. Papathanassiou, and S. Manias, "Wireless phase–locked loop control for inductive power transfer systems," in *Proc. IEEE Appl. Power Electron. Conf. Expo.*, Mar. 2015, pp. 1601–1607.

[26] W. Zhang, Q. Chen, S-C. Wong, C. K. Tse, and X. Ruan, "A novel transformer for transcutaneous energy transmission systems," in *Proc. IEEE Energy Conv. Congr. Exp.*, 2009, pp. 3218–3224.

[27] D. K. W. Cheng, L. P. Wong, and Y. S. Lee, "Design, modeling and analysis of integrated magnetics for power converter," in *Proc. IEEE Power Electron. Spec. Conf.*, 2009, pp. 320–325.

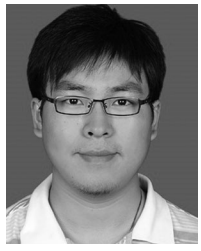

Ligang Xu (S'15) received the master's degree in electrical engineering, in 2009, from Nanjing University of Aeronautics and Astronautics, Nanjing, China, where he is currently working toward the Ph.D. degree in electrical engineering.

His current research interests include contactless resonant converters and wireless power transfer system.

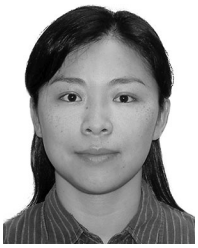

Qianhong Chen (M'06) received the B.S., M.S., and Ph.D. degrees in electrical engineering from Nanjing University of Aeronautics and Astronautics (NUAA), Nanjing, China, in 1995, 1998, and 2001, respectively.

In 2001, she joined the Teaching and Research Division of the Faculty of Electrical Engineering at NUAA, Nanjing, China, and is currently a Professor with the Aero-Power Sci-Tech Center, College of Automation Engineering. From April 2007 to January 2008, she was a Research Associate in the Department of Electronic and Information Engineering, Hong Kong Polytechnic University, Hong Kong, China. Her research interests include application of integrated-magnetics, inductive power transfer converters, soft-switching dc–dc converters, power factor correction, and converter modeling. She has published more than 70 papers in international journals and conferences, and is the holder of 13 patents.

Xiaoyong Ren (S'04–M'11) received the B.S., M.S., and Ph.D. degrees in electrical engineering from the Nanjing University of Aeronautics and Astronautics, Nanjing, China, in 2002, 2005, and 2008,respectively.

From 2009 to 2011, he was a Postdoctoral Researcher at the Center for Power Electronics Systems, Virginia Polytechnic Institute and State University, Blacksburg, VA, USA. He is currently with the Department of Electrical Engineering, NUAA. He has authored and coauthored more than 30 technical papers published in international journals and conference proceedings. His current research interests include dc–dc conversion, converter control techniques, GaN device application, and renewable power systems.

Siu-Chung Wong (M'01–SM'09) received the B.Sc. degree in physics from the University of Hong Kong, Hong Kong, in 1986, the M.Phil. degree in electronics from the Chinese University of Hong Kong, Hong Kong, in 1989. With the support of The Hong Kong Polytechnic University from 1993 to 1997, he received the Ph.D. degree at The University of Southampton, United Kingdom in 1997.

He joined the Hong Kong Polytechnic in 1988 as an Assistant Lecturer. He is currently an Associate Professor in the Department of Electronic and Information Engineering, The Hong Kong Polytechnic University, where he conducts research in power electronics. From 2012 to 2015, he was appointed as a Chutian Scholar Chair Professor by the Hubei Provincial Department of Education, China, and the appointment was hosted by Wuhan University of Science and Technology, Wuhan, China. In 2013, he was appointed as Guest Professor by the School of Electrical Engineering, Southeast University, Nanjing, China. He was a Visiting Scholar at the Center for Power Electronics Systems, Virginia Tech, VA, USA, in November 2008, Aero-Power Sci-tech Center, Nanjing University of Aeronautics and Astronautics, Nanjing, China, in January 2009, and School of Electrical Engineering, Southeast University, Nanjing, China, in March 2012.

Dr. Wong is a Member of the Electrical College, The Institution of Engineers, Australia. He serves as an Editor of the *Energy and Power Engineering Journal* and a Member of the Editorial Board of the *Journal of Electrical and Control Engineering*. He serves as a Guest Associate Editor of IEEE JOURNAL OF EMERGING AND SELECTED TOPICS IN POWER ELECTRONICS, Special Issue on Power Electronics for Biomedical Applications, 2014. He serves as an Associate Editor of IEEE TRANSACTIONS ON CIRCUITS AND SYSTEMS-II: EXPRESS BRIEFS.

Chi K. Tse (M'90–SM'97–F'06) received the B.Eng. (Hons.) degree with first class honors in electrical engineering, and the Ph.D. degree from the University of Melbourne, Australia, in 1987 and 1991, respectively.

He is presently the Chair Professor at the Hong Kong Polytechnic University, Hong Kong, with which he served as Head of the Department of Electronic and Information Engineering from 2005 to 2012. He has author/co-author 10 books, 20 book chapters and more than 500 papers in research journals and conference proceedings, and holds 5 US patents.

Dr. Tse received a number of research and industry awards, including the Prize Paper Awards by IEEE TRANSACTIONS ON POWER ELECTRONICS in 2001 and 2015, the *RISP Journal of Signal Processing* Best Paper Award in 2014, the Best paper Award by *International Journal of Circuit Theory and Applications* in 2003, two gold medals at the International Inventions Exhibition in Geneva in 2009 and 2013, and a number of recognitions by the academic and research communities, including the honorary professorship by several Chinese and Australian universities, the Chang Jiang Scholar Chair Professorship, the IEEE Distinguished Lectureship, the Distinguished Research Fellowship by the University of Calgary, the Gledden Fellowship and International Distinguished Professorship-at-Large by the University of Western Australia. While with the Hong Kong Polytechnic University, he received the President's Award for Outstanding Research Performance twice, the Faculty Research Grant Achievement Award twice, the Faculty Best Researcher Award, and several teaching awards. He serves and has served as an Editor-in-Chief for the IEEE TRANSACTIONS ON CIRCUITS AND SYSTEMS II (2016-2017), *IEEE Circuits and Systems Magazine* (2012-2015), Editor-in-Chief of the IEEE CIRCUITS AND SYSTEMS SOCIETY NEWSLETTER (since 2007), Associate Editor for three IEEE Journal/Transactions, Editor for the *International Journal of Circuit Theory and Applications*, and is on the editorial boards of a few other journals. He also serves as a panel Member of Hong Kong Research Grants Council and NSFC, and Member of several professional and government committees.